PCCP



PAPER View Article Online



Cite this: Phys. Chem. Chem. Phys., 2020, 22, 20295

Intrinsic electronic spectra of cryogenically prepared protoporphyrin IX ions in vacuo — deprotonation-induced Stark shifts†

Wyatt Zagorec-Marks, pab James E. T. Smith, Madison M. Foreman, Sandeep Sharma and J. Mathias Weber state

We present electronic spectra containing the Q_x and Q_y absorption bands of singly and doubly deprotonated protoporphyrin IX, prepared as mass selected ions *in vacuo* at cryogenic temperatures, revealing vibronic structure in both bands. We assign the vibronic progression of the Q_x band using a Frank–Condon–Herzberg–Teller simulation based on time-dependent density functional theory, comparing the observed bands with those calculated for porphine. A comparison of the electronic spectra of the two charge states allows investigation of the electronic Stark effect with an electric field strength beyond the capabilities of typical laboratory setups. We analyze the differences in the electronic spectra of the two charge states using n-electron valence perturbation theory (NEVPT2) and simulated charge distributions.

Received 6th July 2020, Accepted 1st September 2020

DOI: 10.1039/d0cp03614e

rsc.li/pccp

Introduction

Porphyrins and metalloporphyrins are a versatile class of macrocycles which are ubiquitous in biology, where they perform important tasks, such as participating in electron/chemical transport, and photosynthesis, among others. Because of their extensive use in biological systems, they have elicited many efforts to utilize them in applications including as photosensitizers in solar cells, hotocatalysts for CO₂ reduction, and as candidates for non-linear optical materials to name just a few. These applications center around the intense visible absorption bands that are characteristic of porphyrins. Optimizing such applications requires a thorough understanding of their intrinsic electronic structure, as well as how their interactions with their chemical environment change their properties.

The core structure is a conjugated ring consisting of four pyrrole rings connected by methine bridges. The simplest way to understand the electronic spectrum of porphyrins is to treat the $18~\pi$ electrons of the porphyrin ring as particles on a ring.

Scheme 1 $D_{\rm 4h}$ and $D_{\rm 2h}$ macrocycle structures and their schematic electronic spectra for a general metalloporphyrin (left) and protoporphyrin IX (right).

This treatment leads to the four orbital model by Gouterman^{8,9} which predicts one degenerate pair of weak transitions, referred to as the Q band, and one degenerate pair of more intense transitions, referred to as the B or Soret band. The Q band is always accompanied by a vibronic progression and appears in low-resolution spectra as two peaks spaced by ca. 1500 cm⁻¹. This basic spectral feature (see Scheme 1) is referred to as the D_{4h} signature, and is observed in electronic spectra of metalloporphyrins where the macrocycle has approximate D_{4h} symmetry. If the metal center is removed and two of the nitrogen atoms are protonated, the symmetry of the macrocycle is lowered to D_{2h} , and the degeneracy of the electronic state giving rise to the

Path D2h D2h Aisuati.

^a JILA, University of Colorado, Boulder, CO 80309, USA

b Department of Chemistry, University of Colorado, Boulder, CO 80309, USA. E-mail: weberjm@jila.colorado.edu

 $[\]dagger$ Electronic supplementary information (ESI) available: Links to the input files for all correlated calculations and the scripts use to generate several of the figures; details of correlated calculations; discussion of model PP (PP-Me) with point charges; Franck–Condon simulation of porphine; solvatochromic data for PP; mid IR spectra of PP anions; full list of frequencies and intensities of vibrational modes in the Q_x band of porphine and (PP–H) $^-$; animations of key vibrational modes in the Q_x band of porphine and [PP–H] $^-$. See DOI: 10.1039/d0cp03614e

Paper

Q band is lifted. In this case, one instead observes two components, referred to as Q_x and Q_y bands as well as the analogous B_x and B_y bands, and this pattern is referred to as the free-base or D_{2h} electronic signature. Typically the splitting in the B bands is too small to be observed. This is the case in protoporphyrin IX (PP), (see Scheme 1) which is the focus of this work.

The electronic structure of porphyrin systems has been studied for decades, 8,10-13 including that of PP. 14 Many of these experiments, however, have been performed in solutions and at room temperature, where vibronic structure is largely obscured by hot bands and solvent effects. In addition, the amphiphilic nature of PP results in the formation of generally polydisperse aggregates in aqueous solution, whose number of monomer units varies with pH.15 As a result, condensed-phase experimental data on the electronic structure of PP do not reflect the intrinsic properties of this chromophore. Brøndsted-Nielsen and coworkers¹⁶ performed spectroscopy on PP in vacuo at room temperature, but they were not able to observe the lowest energy part of the Q_r signature, and the features in the spectra suffered from broadening and spectral congestion due to hot bands. Similarly, supersonic jet experiments of neutral PP showed significant spectral congestion, 17 likely due to incomplete vibrational cooling. In cryogenic matrices, 8,14 each absorption feature appears as a multiplet, due to matrix effects. While these cryogenic experiments did provide vibronic resolution, the multiplet structure complicated the interpretation of the spectra, and a detailed characterization of the intrinsic electronic spectrum of PP remains elusive.

Electronic spectroscopy of mass selected ions in vacuo circumvents problems arising from aggregation or effects of the chemical environment, such as a matrix or solvent. This approach provides insight into the intrinsic photophysical properties of a molecule, and it has been employed by several groups to great success. 16,18-32 In addition, preparing the target ions at cryogenic temperatures suppresses broadening effects from hot bands, allowing for the best possible detail to be extracted from the spectra. In this work, we present electronic spectroscopy of cryogenically prepared singly and doubly deprotonated PP ions. Together with the absence of solventinduced charge screening, the selection of the charge state allows us to study the electronic Stark effect induced by electric fields of a charge located only a few Å away from the conjugated macrocycle, which are on the order of 10⁹ V m⁻¹. We compare our experimental data with calculations on both PP and porphine in the framework of time-dependent density functional theory (TDDFT) and complete active space self-consistent field (CASSCF) calculations with strongly contracted n-electron valence state perturbation theory (NEVPT2) corrections.

Experimental

The experimental apparatus has been described in detail elsewhere.³³ Briefly, a 0.5 mM solution of protoporphyrin IX disodium salt (Sigma-Aldrich, >90% purity) was prepared in a 1:1 methanol:water mixture, with the pH adjusted by addition

of KOH solution to pH 12. The solution was electrosprayed without further purification. The ions were guided by octopole ion guides through a series of differential pumping stages and injected into a cryogenic Paul trap. The trap temperature was held at 30 K, and He was pulsed into the trap as buffer gas. Ions cooled down in collisions with the buffer, which allowed formation of weakly bound van der Waals complexes of deprotonated PP ions with residual N2 molecules, whose binding energy can be estimated to ca. 500 cm⁻¹. The N₂ molecules allow the use of messenger spectroscopy, and their presence also sets an upper limit on the internal energy content of the complex (equivalent to ca. 60 K), and thus guarantees the PP ions are cold. The ions were held in the trap for 50 ms to allow sufficient time for cooling and complex formation, after which they were injected into a reflectron-time-of-flight mass spectrometer. After mass separation in the first stage of the mass spectrometer, the ions of interest were mass selected by a pulsed mass gate and irradiated by the output of a tunable optical parametric converter. Electronic spectra were acquired using a BBO based optical parametric oscillator (5-7 ns pulse duration, 5 cm⁻¹ bandwidth), while a KTP/KTA/AgGaSe₂ based optical parametric converter was used to measure vibrational spectra (5-7 ns pulse duration, 2 cm⁻¹ bandwidth). Photodissociation action spectra were obtained by monitoring the loss of the weakly bound N2 messenger molecules. The action channel for all experiments is the single-photon induced loss of a single, weakly bound N2 molecule from a complex of the form $[(PP-nH)^{n-}\cdot N_2]$ (n = 1, 2). Care was taken to ensure that the transitions were not saturated.

Computational

Geometry optimization and harmonic vibrational frequency calculations for both the ground state and the S_1 state (*i.e.*, the Q_x band) of porphine and PP were performed with density functional theory (DFT) and TDDFT, respectively, employing the CAM-B3LYP³⁴ functional with cc-pVDZ³⁵ basis sets for all atoms. Vertical transition energies of the S_1 and S_2 states (*i.e.*, the Q_x and Q_y bands) were calculated for geometries of several charge states of PP using both the ω B97XD³⁶ and CAM-B3LYP functionals with cc-pVDZ basis sets after optimization using the same methods and basis sets. All DFT and TDDFT calculations were performed using Gaussian 16.³⁷

The ground and excited state results were used to obtain Franck-Condon-Herzberg-Teller (FCHT) simulations. ¹² We note that the construction of a Duschinsky rotation for PP without further approximations failed, and we therefore used the vertical gradient approximation ³⁸ to calculate the FCHT simulation for the vibronic spectrum of PP in the S₁ state. We interpret our experimental spectrum through comparison with a FCHT simulation for porphine, which serves as a model system for the conjugated system of PP, and the FCHT simulation of PP within the vertical gradient approximation as described above. The temperature for all reported FCHT simulations was zero K.

PCCP Paper

In addition to the single-reference methods mentioned above, we used multireference methods to calculate the vertical excitation energies. Previous work has shown that CASSCF/ NEVPT2 calculations predict the excitation energies of the two Q bands well, 39,40 and Angeli et al. note that an active space of 4 electrons in 4 orbitals (4e,4o) provides a nearly quantitative splitting of the Q bands. 41 For all reference wave functions we use an active space consisting of the two highest (and lowest) lying doubly occupied (and unoccupied) π -orbitals from the conjugated system around the porphyrin ring. We generated reference wave functions using state averaged CASSCF, abbreviated as SA-N-CASSCF where N is the number of states included in the average; the energies of these wave functions were corrected using strongly contracted N-electron valence perturbation theory. 42-44 We tested averaging 3 states

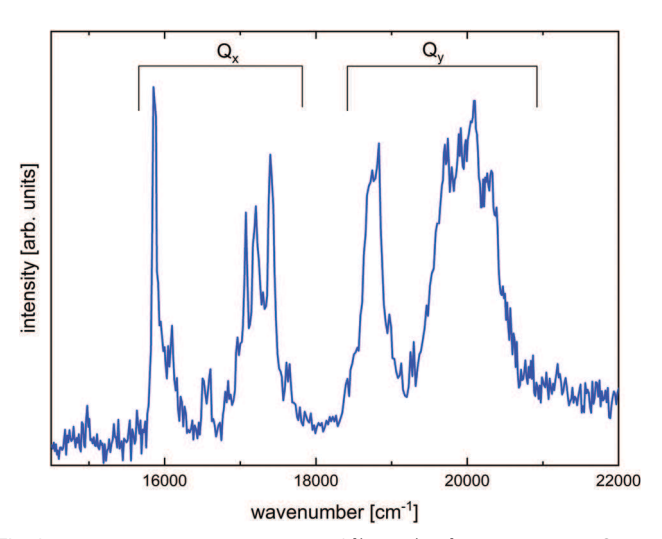


Fig. 1 Photodissociation spectrum of $[(PP-H)\cdot N_2]^-$, showing the Q_x and Q_v absorption bands. The Q_x band origin is at 15 868 \pm 10 cm⁻¹, and the Q_v band origin is at $18760 \pm 30 \text{ cm}^{-1}$. Both band origins are followed by a vibronic progression that extends ca. 2000 cm⁻¹ above the origin.

(ground, Q_x , and Q_y) and 5 states (ground, Q_x , Q_y , B_x , and B_y); both produced qualitatively similar results with the N = 3 case yielding the best agreement with experiment, so we report those results here. All correlated calculations used the cc-pVDZ basis set and were performed using the PySCF45-47 package and checked with the ORCA^{48,49} package. The PySCF results are reported in this work and the ORCA results are included in the ESI.† The input files necessary to reproduce all correlated calculations are freely available on GitHub (see ESI,† Section S1 for more details).

Results and discussion

Fig. 1 shows the photodissociation spectrum of the $[(PP-H)\cdot N_2]^{-1}$ complex in the Q_x and Q_y band regions. The Q_x band origin is at 15 868 \pm 10 cm⁻¹ and is followed by a vibronic progression that will be discussed below. The Q_{ν} band origin is at 18 760 \pm 30 cm $^{-1}$. The Q_{ν} band has a similar vibronic progression, but it is less resolved, likely due to a shorter excited state lifetime. We note that the experimental spectrum fails to return to baseline on the high energy end of the spectrum recorded here. We attribute this observation to the onset of the Soret band. Exploratory measurements on complexes with two nitrogen molecules attached indicate that the N2-induced shift of the band origin is ca. 10 cm⁻¹ per N₂ adduct.

Table 1 shows a comparison of experimental and calculated vertical transition energies, which represent the band origins, according to simple Franck-Condon simulations (see ESI†). The TDDFT calculations generally overestimate the Q_x band origin energy, but underestimate the Q_v band origin energy, and the resulting calculated Q_x - Q_y splitting is roughly half of the experimentally observed value. The orbitals contributing to the transitions in the monoanion are located in the macrocycle, as expected (see ESI†). We note that the TDDFT transitions for the dianion contain charge transfer contributions from the

Table 1 Calculated and experimental vertical transition energies in cm⁻¹

Species	Charge state	Method ^a	$E(\mathbf{Q}_x)^b$	$E(Q_y)^b$	ΔE^c
Porphine	0	CAM-B3LYP	17 500	19321	1821
	0	ωB97XD	17 029	18 926	1897
PP	0	Experiment ^d	15900 ± 100	19050 ± 100	3150 ± 141
	0	CAM-B3LYP	17 312	18738	1426
	0	NEVPT2	15 810	18 606	2796
	-1	Experiment ^e	15870 ± 10	18760 ± 30	2890 ± 32
	-1	CAM-B3LYP	16 923	18 426	1503
	-1	ωB97XD	16 518	18 095	1577
	-1	NEVPT2	15 377	18 217	2840
	-2	Experiment e	$15760\pm10\;(-110)$	$18270\pm30\ (-490)$	2510 ± 32
	-2	CAM-B3LYP	16 970 (+452)	18 240 (-186)	1270
	-2	ωB97XD	16 660 (+142)	18 048 (-47)	1388
	-2	NEVPT2	15 472 (+95)	18 123 (-94)	2651

^a See Methods section for basis sets. ^b Numbers in parentheses represent the shift of bands in the diamon from the position of each band in the monoanion. ^c ΔE refers to the Q_x-Q_y splitting: $\Delta E=E(Q_y)-E(Q_x)$. ^d Supersonic jet experiment, from ref. 17. ^e The band origins (adiabatic transition energies) set the lower limit for the vertical transition energies. Since the experimental spectra indicate that the band origins have the greatest intensities, we assign them as the vertical transition energies, in order to compare them with the vertical energies from the calculations.

PCCP Paper

carboxylate groups to the macrocycle, despite the fact that both functionals used here are range-corrected. This makes the dianion results in the TDDFT framework questionable. The NEVPT2 calculations generally underestimate both Q_r and Q_v band energies, but are in better agreement with the experimentally observed Q_r-Q_v splitting for all charge states. The active space consists of orbitals localized on the macrocycle, so the electronic transitions only involve the excitation of electrons among these orbitals, and the carboxylate groups are therefore not directly involved in the excitations (by design). We show the active space orbitals along with the leading configurations for each state in the ESI.†

Fig. 2 shows the Q_x band of the photodissociation spectrum of the [(PP-H)·N₂] complex (blue trace) along with the FCHT simulations for porphine (black trace) and (PP-H) (green trace), the latter using the vertical gradient approximation.

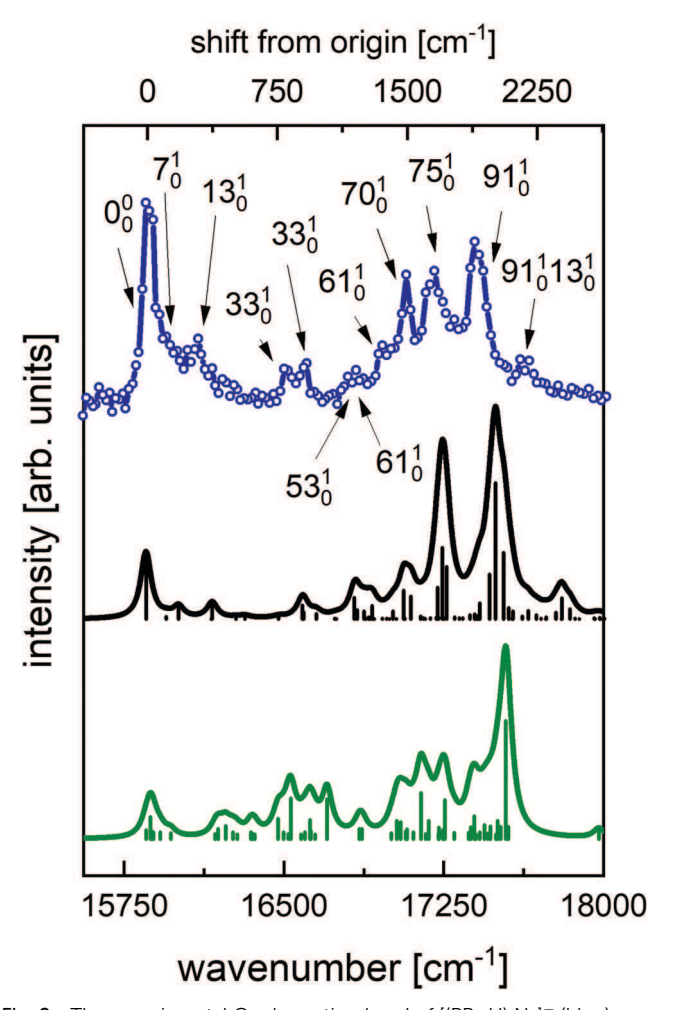


Fig. 2 The experimental Q_x absorption band of $[(PP-H)\cdot N_2]^-$ (blue) compared with the FCHT simulation of neutral porphine (black), and FCHT calculation of (PP-H) vertical gradient approximation (green). Both calculations were done at the CAM-B3LYP/cc-pVDZ level of theory with a scaling factor of 0.97 to account for anharmonicity. The open circles are data points, the full line is a B-spline to guide the eye. The assignments are based on the porphine simulation. The simulations have been shifted to align with the experimental band origin.

While both FCHT simulations are in reasonable agreement with the experimental spectrum, the porphine simulation recovers the experimental spectrum better. This suggests that the observed progression is primarily due to excitations in vibrational modes of the macrocycle, and we hypothesize that inclusion of the side chains in the calculations introduces more coupling between the conjugated system and the side chains than is experimentally observed. We note that the Herzberg-Teller treatment underestimates the relative intensity of the band origin, but is closer to the experimental band envelope, compared to simple Franck-Condon simulations, as stated previously by others. 12 The simpler Franck-Condon calculations establish the vertical transition energies at the band origin, in agreement with the experimental spectra. Mode assignments below are based on the porphine simulation and are presented as M_a^b where M is the vibrational mode, a is the number of quanta in the ground state, and b is the number of quanta in the excited state (see ESI† for assignment based on [PP-H] FCHT simulation with vertical gradient approximation).

The Q_x band origin of $[(PP-H)\cdot N_2]^-$ at 15 868 \pm 10 cm⁻¹ is followed by a vibronic progression that extends until ca. 18 000 cm⁻¹. The band origin is accompanied by two close-lying features, a shoulder at 77 cm⁻¹ and a peak at 227 cm⁻¹ above the band origin. The shoulder corresponds to the 7_0^1 band. This is a macrocycle deformation mode where elongation along the x-axis is out of phase with elongation along the y-axis. The in-phase combination of these motions is the 13¹ band and is responsible for the peak at 227 cm⁻¹ (see ESI† for animations of key vibrational modes).

There is a set of two peaks at 642 cm⁻¹ and 722 cm⁻¹ above the band origin which are the 33_0^1 and 41_0^1 bands, respectively. These include deformations of the pyrrole rings, together with distortions of the macrocycle. At this point in the progression, ca. 1000 cm⁻¹ from the origin, significant spectral congestion sets in as a result of multiple FCHT active states close in energy. The remaining assignments are based on the states with the largest FCHT factors, but we note that many of the weaker transitions are likely unresolved shoulders in the experimental spectrum and certainly contribute to the overall band pattern. The 53_0^1 and 61_0^1 bands give rise to partially resolved features centered around 972 cm⁻¹. Mode 53 is again a combination of pyrrole and macrocycle deformations, while mode 61 is an inplane pyrrole CH wagging mode. The 68¹₀ band which appears at 1102 cm⁻¹ is a methine CH wagging mode.

The three intense peaks at 1202 cm⁻¹, 1332 cm⁻¹, and 1532 cm⁻¹ primarily correspond to bands 70_0^1 , 75_0^1 , and 91_0^1 respectively. Mode 70 is predominantly an in-plane NH bending motion, mode 75 is a CN stretching motion combined with methine CH wagging, and mode 91 is a CC stretch involving the bridging carbons combined with NH wagging.

Deprotonation of one of the carboxylic acid groups in PP results in a negative excess charge ca. 4 Å from the rim of the conjugated macrocycle, producing an electric field strength on the order of 109 V m⁻¹. The Stark effect from this electric field shifts the electronic energy levels of the molecule. Because our experiment is limited to ions, we cannot measure the spectrum

PCCP Paper

of neutral PP. We can, however, deprotonate one or both carboxylic groups of PP and investigate the effect of moving from a singly deprotonated (monoanion) to a doubly deprotonated PP (dianion). In addition to doubling the overall charge of the ion, the mono- and dianion can be expected to have different structures, since the excess charges on the carboxylate groups in the dianion will repel each other. This necessitates a structural investigation for the two different deprotonation states to fully characterize the geometric and electronic structures of the two ion states.

The structures of $[(PP-H)\cdot N_2]^-$ and $[(PP-2H)\cdot N_2]^{2-}$ were determined using vibrational spectroscopy. Fig. 3 shows the spectra of $[(PP-H)\cdot N_2]^-$ and $[(PP-2H)\cdot N_2]^{2-}$ in the fingerprint region from 1000 cm⁻¹ to 2200 cm⁻¹ along with the simulated harmonic spectrum of the lowest energy structure of each species determined in a structural search. In the structure used to generate the simulated spectrum of the monoanion (upper trace), the two carboxylate groups share the remaining proton of the two carboxylic acid groups. Overall, the simulation matches the experimental spectrum well. The peaks at 1726 and 1617 cm⁻¹ are the antisymmetric OCO stretching vibrations for the two carboxylate groups. The feature at 1617 cm⁻¹ is accompanied by an unresolved shoulder at ca. 1592 cm⁻¹ corresponding to two CC stretching vibrations of the ethylene

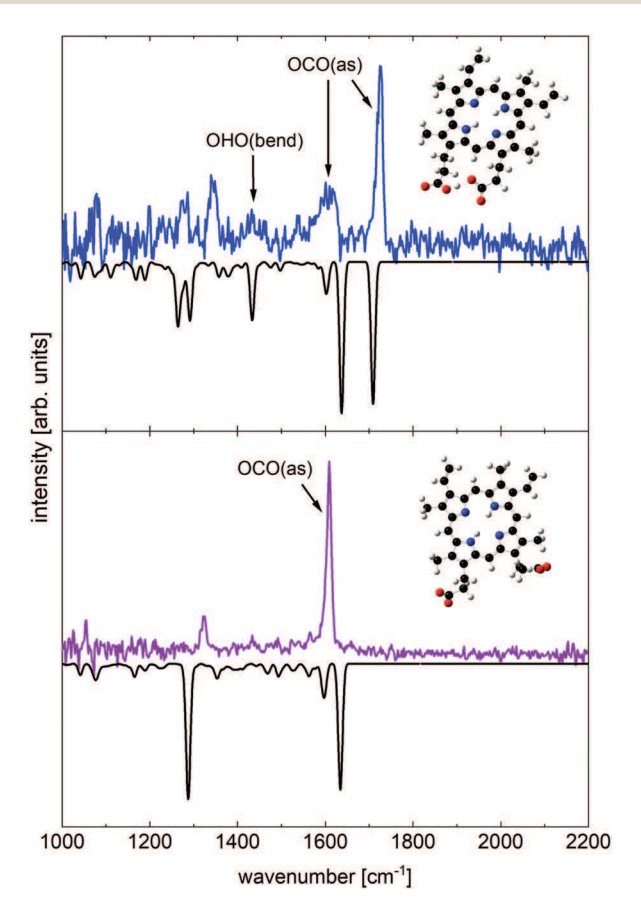


Fig. 3 Vibrational spectrum of $[(PP-H)\cdot N_2]^-$ (blue) and $[(PP-2H)\cdot N_2]^{2-}$ (purple) along with calculated harmonic spectra (black) of the structures shown (scaling factor 0.95)

groups. The broad feature at 1430 cm⁻¹ is the OHO bending mode involving the shared proton. The final two features we assign are the pair of peaks at 1280 and 1245 cm⁻¹. These are HCH bending modes localized on the propionic acid chains.

The lower trace of Fig. 3 shows the vibrational spectrum of $[(PP-2H)\cdot N_2]^{2-}$. Instead of two clearly resolved antisymmetric OCO stretching vibrations observed for the monoanion, we now observe a single feature at 1609 cm⁻¹. This feature contains the unresolved antisymmetric OCO stretching signatures of both carboxylic groups, which are of similar intensity. The CC stretching vibrations of the ethylene groups again occur as a shoulder on the low energy side of the OCO stretching peak. The HCH bending modes localized on the propionic acid chains, which were two separate features in the spectrum of the monoanion, have also collapsed into a single feature at 1324 cm⁻¹. The observation that both the OCO stretching peaks and the HCH bending signatures now only show single features reflects the fact that the two propionic acid chains with the carboxylate groups are now nearly completely decoupled. This observation is reminiscent of work by Johnson and coworkers⁵⁰ on mono- and dicarboxylate anions of dodecanedioic acid, where the signatures of the monoanion species are significantly more complex than for the dianion, as the carboxylate groups in the former also share a proton, while the two carboxylate groups become decoupled in the latter. We note that the OHO bending mode is no longer present, since both carboxylate groups are now deprotonated. The structure shown for the dianion in Fig. 3 is the lowest energy isomer of four that produce nearly identical vibrational spectra. This isomer has one carboxylate group on the left in the figure below the plane defined by the macrocycle, and the other above that plane. The other three are different combinations of each carboxylate group being above or below the plane defined by the macrocycle, and all lie within 30 meV of the structure shown.

In many cases, cryogenic ion spectroscopy in vacuo allows the determination of solvatochromic shifts. Unfortunately, this is not the case for PP in aqueous solutions since PP forms aggregates due to its amphiphilic character. Only at low pH (<3) are monomers the only solute species, but p K_a values of similar molecules⁵¹ suggest that PP should be neutral in this range. As a result, shifts observed upon bringing PP into a solvent are the results of several effects: (i) solvatochromic effects due to the differential solvation of the charge distributions; (ii) aggregation induced shifts; (iii) charge screening effects that change the impact of the intramolecular electric field coming from deprotonated propionic acid groups. These effects cannot easily be disentangled, and we therefore refrain from a more detailed discussion in this vein, but provide a comparison of the current data with literature data on solutions in ESI.†

The local electric field from the charged side groups on the macrocycle most likely plays the main role in the observed band shifts through the Stark effect. Spectroscopy in vacuo is ideal to investigate the influence of the local field, since there is no dielectric screening through solvent effects, and direct comparison with theoretical methods is therefore straightforward.

Paper PCCP

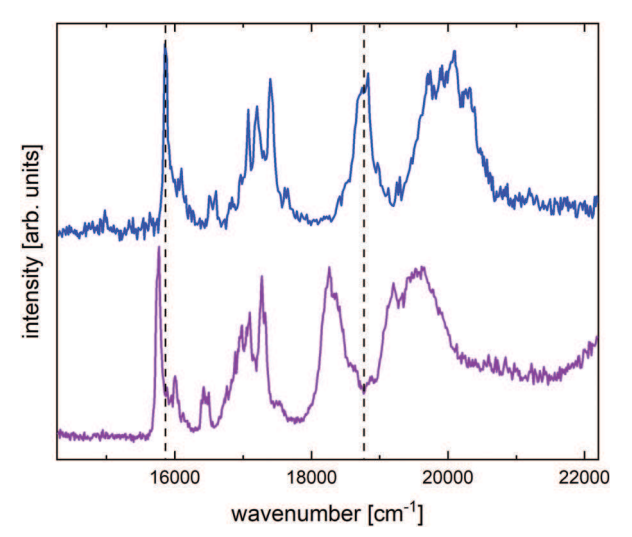


Fig. 4 Electronic spectrum of $[(PP-H)\cdot N_2]^-$ (blue) and $[(PP-2H)\cdot N_2]^{2-}$ (purple) in the Q band region. Dashed vertical lines mark the origin positions of the Q_x and Q_y bands of the singly deprotonated species to emphasize the shifts with the increase in electric field strength.

Fig. 4 shows the electronic spectra of singly and doubly deprotonated PP to illustrate the differences induced by the change in the local electric field. The two spectra are qualitatively very similar, with slight changes in the spacing of the Q_x and Q_{ν} bands and in the relative intensities of a few features of their vibronic progressions. This similarity is not surprising, because the structure of the conjugated macrocycle has not changed substantially. Experimental data from the literature on neutral PP in the gas phase¹⁷ have relatively large error bars compared to our results, but the data suggest that the Q_x band shifts very little to the red upon loss of a single proton, while the Q_v band shifts by ca. -300 cm^{-1} , reducing the Q_x-Q_v splitting (see Table 1). The Q_x band in the dianion spectrum shifts by -110 cm^{-1} relative to the monoanion spectrum, while the Q_{ν} band shifts by -490 cm^{-1} , again reducing the splitting between the two bands. We also note that we observe the onset of the Soret band at 22 000 cm⁻¹ more clearly in the spectrum of the doubly deprotonated species.

As mentioned above, in contrast to TDDFT, the NEVPT2 calculations on PP recover the overall band positions and splittings quite well. However, even these high-level calculations are unable to reproduce the more subtle changes introduced by the change in charge state. The NEVPT2 calculations predict a red shift for the Q_x band going from neutral PP to the monoanion, and they yield a blue shift as the charge state is changed from -1 to -2 (see Table 1). The calculated Q_x-Q_y splitting first becomes wider (from charge state 0 to -1), then narrower again (from -1 to -2). Calculations on a simplified model structure that is placed in the field of point charges approximating the charge distribution of the ions are also unable to recover the experimental trends (see ESI†). The comparison of computational and experimental results highlights the difficulties that molecules such as PP present to even high-level computational treatments and shows how cryogenic ion spectroscopy experiments can serve as benchmarks for increasingly sophisticated, computationally demanding theory.

Conclusions

We have measured the intrinsic electronic spectra of singly and doubly deprotonated PP in the region of the Q_x and Q_y bands, as well as the infrared spectra of these ions in the fingerprint region. Cryogenic preparation of the ions and the use of N₂ messenger tags allow us to observe detailed vibrational structure in the electronic bands, separate from any effects of solvents or aggregation. Based on the infrared spectra, we assign a unique structure for the singly deprotonated species exhibiting a shared proton between the two propionic acid groups. In doubly deprotonated PP, Coulomb repulsion between the two charged groups results in near-complete decoupling of the vibrational modes localized on the two acid groups. The vibrational properties in both the ground state and the Q_x band are well recovered based on DFT calculations, with TDDFT/FCHT simulations on porphine allowing a detailed vibronic analysis of the Q_r band. The observed differences between the electronic spectra of the two deprotonation states are mainly due to the Stark effect (local electric field strengths are on the order of 10⁹ V m⁻¹), caused by the negative charge(es) on the propionic acid side chains. The splittings between the Q_r and Q_ν bands are nearly quantitatively recovered by NEVPT2 calculations on PP in the different deprotonation states, within a few 10 cm $^{-1}$ for the monoanion, and ca. 140 cm $^{-1}$ for the dianion. However, they fail to predict the more subtle changes in the spectra associated with the Stark effect. The vibronically resolved data in the present work can serve as a benchmark for future theoretical work on porphyrinic molecules.

Conflicts of interest

There are no conflicts to declare.

Acknowledgements

We gratefully acknowledge support from the U. S. National Science Foundation under award no. CHE-1764191. This work utilized resources from the University of Colorado Boulder Research Computing Group, which is supported by the National Science Foundation (awards ACI-1532235 and ACI-1532236), the University of Colorado Boulder, and Colorado State University. S. S. acknowledges funding from the NSF award CHE-1800584 and a Sloan Research Fellowship. J. E. T. S. gratefully acknowledges support from a fellowship through The Molecular Sciences Software Institute under NSF Grant ACI-1547580.

Notes and references

C. U. Carlsen, J. K. S. Møller and L. H. Skibsted, *Coord. Chem. Rev.*, 2005, 249, 485–498.

PCCP

pp. 51-115.

2 V. A. Mamedov and A. A. Kalinin, in *Advances in Heterocyclic Chemistry*, ed. A. R. Katritzky, Academic Press, 2014, vol. 112,

- 3 A. Yella, H.-W. Lee, H. N. Tsao, C. Yi, A. K. Chandiran, M. K. Nazeeruddin, E. W.-G. Diau, C.-Y. Yeh, S. M. Zakeeruddin and M. Grätzel, *Science*, 2011, 334, 629–634.
- 4 S. H. Kang, M. J. Jeong, Y. K. Eom, I. T. Choi, S. M. Kwon, Y. Yoo, J. Kim, J. Kwon, J. H. Park and H. K. Kim, *Adv. Energy Mater.*, 2017, 7, 1602117.
- 5 S. Lin, C. S. Diercks, Y.-B. Zhang, N. Kornienko, E. M. Nichols, Y. Zhao, A. R. Paris, D. Kim, P. Yang, O. M. Yaghi and C. J. Chang, *Science*, 2015, 349, 1208–1213.
- 6 C. Costentin, S. Drouet, M. Robert and J.-M. Saveant, *Science*, 2012, 338, 90–94.
- 7 F. Tessore, A. O. Biroli, G. Di Carlo and M. Pizzotti, *Inorganics*, 2018, **6**, 81.
- 8 M. Gouterman, in *The Porphyrins*, ed. D. Dolphin, Academic Press, 1978, vol. 3, pp. 1–165.
- 9 M. Gouterman, J. Mol. Spectrosc., 1961, 6, 138-163.
- 10 J. M. S. Lopes, K. Sharma, R. N. Sampaio, A. A. Batista, A. S. Ito, A. E. H. Machado, P. T. Araujo and N. M. Barbosa Neto, *Spectrochim. Acta, Part A*, 2019, 209, 274–279.
- 11 C. Rimington, S. F. Mason and O. Kennard, *Spectrochim. Acta, Part A*, 1957, **12**, 65–77.
- 12 F. Santoro, A. Lami, R. Improta, J. Bloino and V. Barone, J. Chem. Phys., 2008, 128, 224311.
- 13 J. G. Radziszewski, J. Waluk, M. Nepras and J. Michl, *J. Phys. Chem.*, 1991, **95**, 1963–1969.
- 14 R. I. Personov and O. N. Korotaev, *Opt. Spectrosc.*, 1971, 32, 900.
- L. M. Scolaro, M. Castriciano, A. Romeo, S. Patane,
 E. Cefali and M. Allegrini, J. Phys. Chem. B, 2002, 106, 2453–2459.
- 16 J. A. Wyer, C. S. Jensen and S. Brøndsted-Nielsen, *Int. J. Mass Spectrom.*, 2011, 308, 126–132.
- 17 J. M. Beames, T. D. Vaden and A. J. Hudson, *J. Porphyrins Phthalocyanines*, 2012, **14**, 314–323.
- 18 G. K. Thurston, C. R. Sagan and E. Garand, *J. Chem. Phys.*, 2019, **151**, 164301.
- 19 J. Roithova, J. Jasik, J. J. Del Pozo Mellado and D. Gerlich, *Faraday Discuss.*, 2019, 217, 98–113.
- 20 Y. Inokuchi, T. Ebata and T. R. Rizzo, J. Phys. Chem. A, 2019, 123, 6781–6786.
- 21 A. Henley and H. H. Fielding, *Int. Rev. Phys. Chem.*, 2019, 38, 1–34.
- 22 S. Daly, M. Porrini, F. Rosu and V. Gabelica, *Faraday Discuss.*, 2019, **217**, 361–382.
- 23 J. C. Chen and R. A. Jockusch, *Phys. Chem. Chem. Phys.*, 2019, 21, 16848–16858.
- 24 C. S. Anstoter, C. W. West, J. N. Bull and J. R. Verlet, *J. Phys. Chem. B*, 2016, **120**, 7108–7113.
- 25 E. B. Jochnowitz and J. P. Maier, *Annu. Rev. Phys. Chem.*, 2008, **59**, 519–544.
- 26 J. Banisaukas, J. Szczepanski, J. Eyler, M. Vala, S. Hirata, M. Head-Gordon, J. Oomens, G. Meijer and G. V. Helden, J. Phys. Chem. A, 2003, 107, 782–793.

- 27 A. Herburger, E. Barwa, M. Oncak, J. Heller, C. van der Linde, D. M. Neumark and M. K. Beyer, *J. Am. Chem. Soc.*, 2019, 141, 18000–18003.
- 28 P. Jager, K. Brendle, E. Schneider, S. Kohaut, M. K. Armbruster, K. Fink, P. Weis and M. M. Kappes, J. Phys. Chem. A, 2018, 122, 2974–2982.
- 29 A. F. DeBlase, C. P. Harrilal, J. T. Lawler, N. L. Burke, S. A. McLuckey and T. S. Zwier, *J. Am. Chem. Soc.*, 2017, 139, 5481–5493.
- 30 J. C. Bopp, E. G. Diken, J. M. Headrick, J. R. Roscioli, M. A. Johnson, A. J. Midey and A. A. Viggiano, *J. Chem. Phys.*, 2006, 124, 174302.
- 31 A. Kaiser, J. Postler, M. Oncak, M. Kuhn, M. Renzler, S. Spieler, M. Simpson, M. Gatchell, M. K. Beyer, R. Wester, F. A. Gianturco, P. Scheier, F. Calvo and E. Yurtsever, J. Phys. Chem. Lett., 2018, 9, 1237–1242.
- 32 L. G. Dodson, W. Zagorec-Marks, S. Xu, J. E. T. Smith and J. M. Weber, *Phys. Chem. Chem. Phys.*, 2018, 20, 28535–28543.
- 33 S. Xu, S. Gozem, A. I. Krylov, C. R. Christopher and J. M. Weber, Phys. Chem. Chem. Phys., 2015, 17, 31938–31946.
- 34 T. Yanai, D. P. Tew and N. C. Handy, *Chem. Phys. Lett.*, 2004, 393, 51–57.
- 35 T. H. Dunning, J. Chem. Phys., 1989, 90, 1007-1023.
- 36 J. D. Chai and M. Head-Gordon, J. Chem. Phys., 2008, 128, 084106.
- 37 M. J. Frisch, G. W. Trucks, H. B. Schlegel, G. E. Scuseria, M. A. Robb, J. R. Cheeseman, G. Scalmani, V. Barone, G. A. Petersson, H. Nakatsuji, X. Li, M. Caricato, A. V. Marenich, J. Bloino, B. G. Janesko, R. Gomperts, B. Mennucci, H. P. Hratchian, J. V. Ortiz, A. F. Izmaylov, J. L. Sonnenberg, D. Williams-Young, F. Ding, F. Lipparini, F. Egidi, J. Goings, B. Peng, A. Petrone, T. Henderson, D. Ranasinghe, V. G. Zakrzewski, J. Gao, N. Rega, G. Zheng, W. Liang, M. Hada, M. Ehara, K. Toyota, R. Fukuda, J. Hasegawa, M. Ishida, T. Nakajima, Y. Honda, O. Kitao, H. Nakai, T. Vreven, K. Throssell, J. A. Montgomery Jr., J. E. Peralta, F. Ogliaro, M. J. Bearpark, J. J. Heyd, E. N. Brothers, K. N. Kudin, V. N. Staroverov, T. A. Keith, R. Kobayashi, J. Normand, K. Raghavachari, A. P. Rendell, J. C. Burant, S. S. Iyengar, J. Tomasi, M. Cossi, J. M. Millam, M. Klene, C. Adamo, R. Cammi, J. W. Ochterski, R. L. Martin, K. Morokuma, O. Farkas, J. B. Foresman and D. J. Fox, Wallingford, CT, 2016.
- 38 A. Baiardi, J. Bloino and V. Barone, *J. Chem. Theory Comput.*, 2013, **9**, 4097–4115.
- 39 K. Falahati, C. Hamerla, M. Huix-Rotllant and I. Burghardt, *Phys. Chem. Chem. Phys.*, 2018, **20**, 12483–12492.
- 40 E. R. Sayfutyarova and S. Hammes-Schiffer, *J. Chem. Theory Comput.*, 2019, **15**, 1679–1689.
- 41 C. Angeli, M. Pastore and R. Cimiraglia, *Theor. Chem. Acc.*, 2007, **117**, 743–754.
- 42 C. Angelo, R. Cimiraglia and J.-P. Malrieu, *Chem. Phys. Lett.*, 2001, **350**, 297–305.
- 43 S. Grimme, J. Antony, S. Ehrlich and H. Krieg, *J. Chem. Phys.*, 2010, 132, 154104.

Paper **PCCP**

- 44 C. Angeli, R. Cimiraglia and J.-P. Malrieu, J. Chem. Phys., 2002, 117, 9138-9153.
- 45 Q. Sun, J. Yang and G. K.-L. Chan, Chem. Phys. Lett., 2017, 683, 291-299.
- 46 Q. Sun, T. C. Berkelbach, N. S. Blunt, G. H. Booth, S. Guo, Z. Li, J. Liu, J. D. McClain, E. R. Sayfutyarova, S. Sharma, S. Wouters and G. K.-L. Chan, Wiley Interdiscip. Rev.: Comput. Mol. Sci., 2018, 8, 1340.
- 47 Q. Sun, X. Zhang, S. Banerjee, P. Bao, M. Barbry, N. S. Blunt, N. A. Bogdanov, G. H. Booth, J. Chen, Z.-H. Cui, J. J. Eriksen, Y. Gao, S. Guo, J. Hermann, M. R. Hermes, K. Koh, P. Koval, S. Lehtola, Z. Li, J. Liu, N. Mardirossian, J. D. McClain, M. Motta, B. Mussard, H. Q. Pham, A. Pulkin, W. Purwanto, P. J. Robinson,
- E. Ronca, E. Sayfutyarova, M. Scheurer, H. F. Schurkus, J. E. T. Smith, C. Sun, S.-N. Sun, S. Upadhyay, L. K. Wagner, X. Wang, A. White, J. D. Whitfield, M. J. Williamson, S. Wouters, J. Yang, J. M. Yu, T. Zhu, T. C. Berkelbach, S. Sharma, A. Sokolov and G. K.-L. Chan, J. Chem. Phys., 2020, 153, 024109.
- 48 F. Neese, Wiley Interdiscip. Rev.: Comput. Mol. Sci., 2017, 8, 1327.
- 49 F. Neese, Wiley Interdiscip. Rev.: Comput. Mol. Sci., 2011, 2, 73-78.
- 50 M. Z. Kamrath, R. A. Relph, T. L. Guasco, C. M. Leavitt and M. A. Johnson, Int. J. Mass Spectrom., 2011, 300, 91-98.
- 51 D. K. Das and O. K. Medhi, J. Inorg. Biochem., 1998, 70, 83-90.